Simulating fundamental and higher harmonic VIV of slender structures (DRAFT)

J. V. Ulveseter, M. J. Thorsen, S. Sævik, C. M. Larsen

Abstract

Vortex-induced vibrations (VIV) of slender marine structures are complicated response processes, where a number of distinct frequency components might be simultaneously active. These are categorized as fundamental and higher harmonics respectively, where the latter can have a tremendous impact on the fatigue life. The present work proposes a method for time domain simulation of such multi-frequency response, by introducing a higher harmonic load term to a pre-existing semi-empirical hydrodynamic force model. Forced motion tests of a circular cylinder were simulated to experimentally and qualitatively validate the fluid-structure energy transfer. Next, the model was used to predict the response of a tension dominated riser in uniform current, for 22 velocities in the range 0.3 m/s to 2.4 m/s. The empirical input was chosen to give an average best fit with respect to the cross-flow strain measurements, which allowed dominating frequencies, fatigue damage, higher harmonics and response variability to be predicted with a high level of realism. Same set of empirical coefficients was subsequently used to predict VIV of three additional flexible pipe experiments in uniform flow, with significant differences in structural properties. The results were satisfactory for all cases, but could be improved by moderate changes to the empirical input.

Keywords:
Time domain, Vortex-induced vibrations, Higher harmonics

1. Introduction

Structural vibrations of bluff bodies associated with flow separation and vortex shedding are commonly named vortex-induced vibrations (VIV). The phenomenon is of particular interest for the oil and gas industry, where offshore production may rely on the performance of slender cylindrical structures. For instance, risers and pipelines can be used for transportation of hydrocarbons, and anchor lines may contribute to positioning of offshore vessels. Such structures are frequently exposed to ocean currents and waves, which makes VIV a potential concern if the vortex shedding frequency is within the range of a natural frequency. If so, fatigue damage due to cyclic stresses over time, and a change of static equilibrium position through drag amplification, can be limiting design factors.

Higher harmonics is an attribute of VIV that significantly shortens the lifetime of slender marine structures, but where limited knowledge has made predictions uncertain. The phenomenon is associated with hydrodynamic loading and response at several simultaneously active frequencies, at the same longitudinal position (here referred to as multi-frequency vortex-induced vibrations). Measurements of riser VIV in current suggest that the higher harmonics appear as multiples of the vortex shedding frequency (e.g. [1, 2, 3]). They distribute differently in the cross-flow and in-line directions (transverse and parallel to the current). Odd multiples are associated with cross-flow vibrations whereas in-line vibrations are characterized by even multiples of the vortex shedding frequency. Experimental studies of spring mounted rigid cylinders have shed light on the hydrodynamics related to higher harmonics [4, 5]. For specific conditions, a new vortex mode 2T was seen to produce lift forces with a distinct component at three times the fundamental frequency. The magnitude of the higher harmonic lift force showed strong dependency on parameters such as the ratio of in-line and cross-flow natural frequency, in-line amplitude, reduced velocity and cylinder trajectory.

Spatial parameter variability, structural properties and stochastic response are some of the factors that influence higher harmonics of flexible pipes. The trajectories and reduced velocity (for non-uniform flow) might vary along the length of the pipe, resulting in an uneven spatial distribution of higher harmonics. The

relative size of bending stiffness and tension also affect the vibration phenomenon. An increase of tension relative to bending stiffness is associated with an increase of higher harmonics (see e.g. [6, 7]). For high mode vibrations, the stochastic nature of VIV becomes evident [8]. The response can jump between periods of stationary mono-frequency vibrations accompanied by higher harmonics, to periods of a broad frequency spectrum, lower amplitudes and a mix of standing and travelling waves [9].

Semi-empirical models are commonly used to predict VIV of slender marine structures. Computational efficiency and (in many cases) sufficient engineering accuracy make them attractive for the industry. These methods rely partly on empirical data to approximate the hydrodynamic loading. Some of the more well-known semi-empirical models are VIVANA [10] and SHEAR7 [11]. Both operate in frequency domain, which restricts analysis to linear structural models in constant flows (i.e. time independent current), and neither of them account for higher harmonic vibrations. To overcome these simplifications, recommended design practice utilize large safety factors to ensure conservative estimates of riser fatigue [12]. There is hence a large potential to decrease over-conservatism by developing models for multi-frequency VIV. The latter has been attempted, assuming lift and drag forces to act in the directions transverse and parallel to the instantaneous inflow felt by the cylinder as it vibrates [13, 14]. However, more experimental validation is needed before any of these semi-empirical models can be considered reliable in predicting multi-frequency VIV. Other proposals to include higher harmonics in fatigue assessment have been made. For example: by suggesting a probabilistic distribution of multi-frequency VIV other than the narrow-banded Gaussian distribution (applicable to frequency domain analysis) [15], and by proposing simplified empirical methods [16, 7].

The present work aims to model fundamental and higher harmonic VIV in time domain. Time domain (as opposed to frequency domain) allows for non-linear structural behaviour and time varying external flow profiles. These features have successfully been included in VIV analysis by Thorsen et al. [17, 18] and Ulveseter et al. [19], but the present study is limited to linear structural models in constant flow. However, they all share the same basis: A semi-empirical time domain formulation of hydrodynamic forces acting on circular cylinders that undergo vortex-induced vibrations. Some modifications have been made since the load model was first published (see e.g. [20, 21, 22]). The force formulation utilized in this paper is a direct extension of the one proposed by Ulveseter et al. [19], which combines Morison's equation with two loading terms that represent the effect of vortex shedding in cross-flow and in-line directions respectively. The latter is subsequently referred to as the fundamental model, since only fundamental frequencies of cross-flow and in-line VIV are directly accounted for.

The new proposal is to extend the fundamental force formulation with an additional hydrodynamic load term. The latter is designed to target higher harmonic lift and drag forces, introducing one additional constant empirical coefficient. The approach is simple, thus the model is only expected to provide an averaged representation of the higher harmonic fluid loads. However, the aim is for the model to be well suitable for engineering applications. In specific, the model should be capable of providing reasonable estimates of the fatigue damage accumulating from multi-frequency VIV of slender structures, knowing that this is vital in engineering design. Based on this, the present paper is mostly devoted to model assessments against experimental data of flexible pipes in current. By simulating four such experiments, we wish to demonstrate that the new coefficient (and the rest of the empirical input) apply to a wide range of cases, and that the structural properties to a large extent govern the higher harmonic response process. The model is also tested under prescribed single-harmonic vibrations, to show that the fundamental fluid-structure power transfer can be well represented despite the new load term. Before these studies are examined, the theoretical basis of the work is presented.

2. Hydrodynamic loading model

The hydrodynamic force on a cylinder strip of unit length is expressed as:

$$\mathbf{F}_n = \underbrace{C_M \rho \frac{\pi D^2}{4} \dot{\mathbf{u}}_n - (C_M - 1)\rho \frac{\pi D^2}{4} \ddot{\mathbf{x}}_n + \frac{1}{2}\rho D C_D |\mathbf{v}_n| \mathbf{v}_n +}_{\text{Morison's equation}}$$

$$\underbrace{\frac{1}{2}\rho D C_{v,y} |\mathbf{v}_n| (\mathbf{j}_3 \times \mathbf{v}_n) \cos\phi_{\text{exc,y}} + \frac{1}{2}\rho D C_{v,x} |\mathbf{v}_n| \mathbf{v}_n \cos\phi_{\text{exc,x}} +}_{\text{Vortex shedding loading terms}} \qquad (1)$$

$$\underbrace{\frac{1}{2}\rho D C_{hh} |\mathbf{v}_n| (\mathbf{j}_3 \times \mathbf{v}_n) \cos(\phi_{\text{exc,y}} + \phi_{\text{exc,x}})}_{\text{Higher harmonic term}}.$$

where the symbols mean:

- ρ: Fluid density.

- D: Cylinder diameter.

- C_M: Inertia coefficient from Morison's equation.

- C_D: Drag coefficient from Morison's equation.

- $C_{v,y}$: Cross-flow vortex shedding force coefficient.

- $C_{v,x}$: In-line vortex shedding force coefficient.

- C_{hh}: Higher harmonic force coefficient.

- $\dot{\mathbf{u}}_n$: Water particle acceleration in the cylinder plane.

- $\ddot{\mathbf{x}}_n$: Cylinder acceleration in the cylinder plane.

- $\mathbf{v}_n$: Relative flow velocity in the cylinder plane defined by $\mathbf{v}_n = \mathbf{u}_n - \dot{\mathbf{x}}_n$.

- $\mathbf{j}_3$: Unit vector in the axial direction.

- $\phi_{\text{exc,y}}$: Instantaneous phase of cross-flow vortex shedding force.

- $\phi_{\text{exc,x}}$: Instantaneous phase of in-line vortex shedding force.

The load model makes use of the cross-flow principle, i.e. both the cylinder and flow velocity/acceleration vectors are decomposed into a normal and tangential part relative to the cylinder strip (labelled by subscript n and t respectively), shown in figure 1. The tangential loads are neglected, which allows us to study the load model in a two-dimensional cylinder plane (i.e. the $\mathbf{j}_1\mathbf{j}_2$-plane in figure 1). In this plane, the forcing terms follow a local axis system where the horizontal axis is parallel to the relative velocity vector $\mathbf{v}_n = \mathbf{u}_n - \dot{\mathbf{x}}_n$. This is illustrated in figure 2, for the load components given by equation 2. Note that the global reference system is defined by the direction of the undisturbed flow velocity alone. Applying the hydrodynamic loads in the local reference system has consequences for which VIV frequencies that can be excited. Details regarding the frequency composition of the load model are found in section 2.2.1.

$$\mathbf{F}_{v,x} = \underbrace{\frac{1}{2}\rho D C_D |\mathbf{v}_n| \mathbf{v}_n + \frac{1}{2}\rho D C_{v,x} |\mathbf{v}_n| \mathbf{v}_n \cos\phi_{\text{exc,x}}}_{\text{Morison's drag + in-line vortex shedding force}}$$

$$\qquad (2)$$

$$\mathbf{F}_{v,y} = \underbrace{\frac{1}{2}\rho D C_{v,y} |\mathbf{v}_n| (\mathbf{j}_3 \times \mathbf{v}_n) \cos\phi_{\text{exc,y}} + \frac{1}{2}\rho D C_{hh} |\mathbf{v}_n| (\mathbf{j}_3 \times \mathbf{v}_n) \cos(\phi_{\text{exc,y}} + \phi_{\text{exc,x}})}_{\text{Cross-flow vortex shedding force + higher harmonics}}.$$
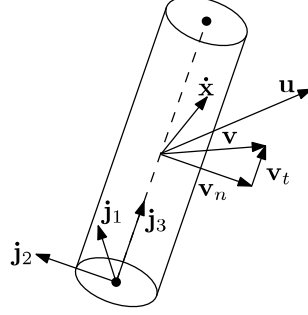
Figure 1: A cylinder segment with local coordinate system and velocity vectors [18].
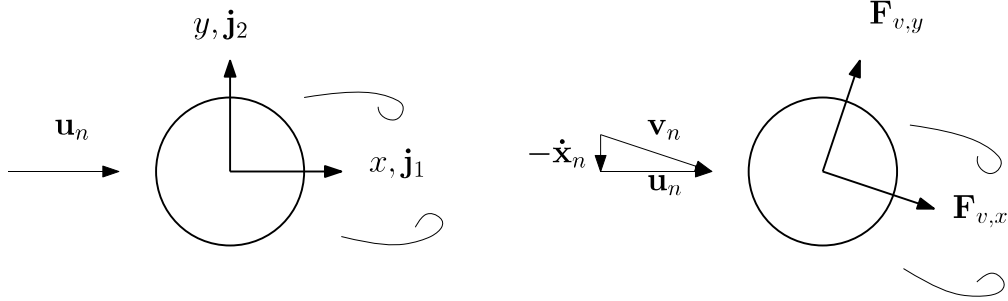

Figure 2: Left: Global reference frame defined by the direction of the undisturbed flow velocity $\mathbf{u}_n$ alone. Right: Local coordinate system defined by the instantaneous direction of the relative velocity $\mathbf{v}_n$.

2.1. Fundamental loading

Equation 1 is based on a synchronization model, where the cross-flow vortex shedding load is able to change its instantaneous frequency to match that of the structural cross-flow response (in the local coordinate system). Synchronization is limited to a range of non-dimensional frequencies referred to as the synchronization range. Outside this interval, the cross-flow vortex shedding force will unsuccessfully try to follow the frequency of structural vibrations, which over time will contribute little to the net energy transfer between the fluid and the structure. Hence, the cross-flow vortex shedding force is able to represent hydrodynamic excitation only when the initial vortex shedding frequency is fairly close to an eigenfrequency. This represents the main physical mechanism of VIV in a simple and effective way. Mathematically speaking, the instantaneous frequency of the cross-flow vortex shedding load is expressed as:

$$\frac{d\phi_{\text{exc,y}}}{dt} = 2\pi f_{\text{exc,y}} = \frac{2\pi |\mathbf{v}_n|}{D} \hat{f}_{\text{exc,y}}, \tag{3}$$

where

$$\hat{f}_{\text{exc,y}} = \hat{f}_0 + \Delta\hat{f}\sin(\phi_{\dot{y}_{\text{rel}}} - \phi_{\text{exc,y}}). \tag{4}$$

$\hat{f}_0$ and $\Delta\hat{f}$ determines the position and span of the synchronization range, respectively, and is part of the empirical input. $\phi_{\dot{y}_{\text{rel}}}$ is the instantaneous phase of the (local) cross-flow structural velocity, and must be numerically approximated for all time steps in a VIV simulation (see Thorsen et al. [18] for details). The numerical model, e.g. finite elements and a time integration scheme of the governing equation, should be refined when higher harmonics are added.

The in-line vortex shedding force can partly synchronize with the (local) in-line response, to excite structural vibrations in the direction of the current. The formulation is somehow different from equation 3 and 4. This, in order to reflect experimental observations suggesting that in-line VIV occur at approximately two times the cross-flow frequency. The instantaneous frequency of the in-line vortex shedding force is given by:

$$\frac{d\phi_{\text{exc,x}}}{dt} = 2\frac{d\phi_{\text{exc,y}}}{dt}[1 + \alpha\sin(\phi_{\dot{x}_{\text{rel}}} - \phi_{\text{exc,x}})], \tag{5}$$

4

where the empirical parameter α determines the rigidity of cross-flow dependency. This means that: $\alpha \to 0 \implies d\phi_{\text{exc,x}}/dt \to 2d\phi_{\text{exc,y}}/dt$. All analyses in this paper are based on $\alpha = 0.15$, which in practise means that the vortex shedding drag load may oscillate at a frequency in the range of 1.7 to 2.3 times the frequency of lift force counterpart.

For accurate predictions of (fundamental) VIV frequencies, the hydrodynamic force proportional to structural acceleration must be realistically represented. The latter is accounted for primarily through the vortex shedding forces and Morison's inertia term. Hence the vortex shedding loads both affect excitation and added mass, as a consequence synchronization. To ensure that VIV is self-limiting, hydrodynamic damping is also included in equation 1. For simplicity, Morison's drag term provides damping in both lateral directions, and for potential higher order frequencies. A realistic representation of the fluid-structure energy transfer is obtained by choosing $C_{v,x}$, $C_{v,y}$ and C_D relative to each other. By including the new higher harmonic term, C_{hh} might also affect the level of excitation, and should therefore be considered together with the coefficients above.

2.2. Higher harmonic loading

Two main considerations have been made in order to formulate the higher harmonic load term:

$$\mathbf{F}_{hh} = \frac{1}{2}\rho DC_{hh}|\mathbf{v}_n|(\mathbf{j}_3 \times \mathbf{v}_n)\cos(\phi_{\text{exc,y}} + \phi_{\text{exc,x}}). \tag{6}$$

These relate to:

1. The frequencies at which the loading distributes.
2. The size of the higher harmonic load components.

2.2.1. Frequency distribution

Let ω denote the fundamental frequency of cross-flow VIV. The cross-flow loading and response should distribute at 3ω, 5ω, 7ω, ..., to represent experimental findings. The in-line frequencies are identified at 2ω, 4ω, 6ω,..., where 2ω denotes the fundamental load/response contribution in the direction parallel to the undisturbed flow. To assess the force model's capacity to represent these frequencies, consider a cylinder strip subjected to a constant current U that undergoes cross-flow and in-line VIV. The following assumptions are introduced as an idealization of the response and loading processes for such a system:

- The global cross-flow structural velocity is a regular sinusoidal time series : $\dot{y}(t) = A_{\dot{y}}\cos\omega t$.

- The global in-line structural velocity is regular and sinusoidal, oscillating at two times the cross-flow frequency and has a phase angle relative to $\dot{y}(t)$, i.e: $\dot{x}(t) = A_{\dot{x}}\cos(2\omega t + \theta)$.

- The instantaneous phases of the cross-flow and in-line vortex shedding forces are given by $\phi_{\text{exc,y}} = \omega t + \theta_y$ and $\phi_{\text{exc,x}} = 2\omega t + \theta_x$, respectively.

In a global reference frame (ref. figure 2), the relative velocity can now be written: $\mathbf{v}_n = (U-\dot{x})\mathbf{j}_1 - \dot{y}\mathbf{j}_2$, where $\mathbf{j}_1$ and $\mathbf{j}_2$ are the in-line and cross-flow unit normals respectively. Furthermore: $\mathbf{j}_3 \times \mathbf{v}_n = \dot{y}\mathbf{j}_1 + (U-\dot{x})\mathbf{j}_2$. Note that all forcing terms in equation 2 are proportional to $(1/2)\rho DC|\mathbf{v}_n| \geqslant 0$ (for different constants C). This factor is a scalar, but may contribute to the frequency distribution of the loading through time variability in $|\mathbf{v}_n|$. In addition comes the effect of the local-global reference frame transformation, which is assessed below:

The cross-flow vortex shedding force, decomposed to the global cross-flow direction, becomes:

$$(U - \dot{x})\cos(\omega t + \theta_y) =$$
$$U\cos(\omega t + \theta_y) - A_{\dot{x}}\cos(2\omega t + \theta)\cos(\omega t + \theta_y) =$$
$$\underbrace{U\cos(\omega t + \theta_y) - \frac{1}{2}A_{\dot{x}}\cos(\omega t + \theta - \theta_y)}_{\text{Fundamental cross-flow frequency}} - \underbrace{\frac{1}{2}A_{\dot{x}}\cos(3\omega t + \theta + \theta_y)}_{3\omega\text{-term}}. \tag{7}$$

The cross-flow vortex shedding force will also contribute to the global in-line force:

$$\dot{y}\cos(\omega t + \theta_y) =$$
$$A_{\dot{y}}\cos\omega t\cos(\omega t + \theta_y) =$$
$$\underbrace{\frac{1}{2}A_{\dot{y}}\cos(2\omega t + \theta_y)}_{\text{Fundamental in-line frequency}} \quad + \quad \underbrace{\frac{1}{2}A_{\dot{y}}\cos\theta_y}_{\text{Drag amplification}} \quad . \tag{8}$$

Similar calculations yield the global cross-flow component of the in-line vortex shedding force:

$$\underbrace{-\frac{1}{2}A_{\dot{y}}\cos(\omega t + \theta_x)}_{\text{Fundamental cross-flow frequency}} \quad \underbrace{-\frac{1}{2}A_{\dot{y}}\cos(3\omega t + \theta_x)}_{3\omega\text{-term}}, \tag{9}$$

and the global in-line component of the in-line vortex shedding force:

$$\underbrace{U\cos(2\omega t + \theta_x)}_{\text{Fundamental in-line frequency}} \quad \underbrace{-\frac{1}{2}A_{\dot{x}}\cos(\theta_x - \theta)}_{\text{Drag amplification}} \underbrace{-\frac{1}{2}A_{\dot{x}}\cos(4\omega t + \theta + \theta_x)}_{4\omega\text{-term}}. \tag{10}$$

Expressions 7 - 10 show that higher harmonic frequencies result from the local-global reference frame transformation of the (fundamental) vortex shedding loads. However, without the additional higher harmonic term, there is no opportunity for independent tuning of the higher order loading. Hence, the new term contributes with modelling flexibility so that the higher harmonic components can be amplified to fit experimental data.

The global cross-flow decomposition of the higher harmonic term is derived in a similar fashion as for the vortex shedding loads:

$$(U - \dot{x})\cos(\phi_{\text{exc,x}} + \phi_{\text{exc,y}}) =$$
$$U\cos(3\omega t + \theta_x + \theta_y) - A_{\dot{x}}\cos(2\omega t + \theta)\cos(3\omega t + \theta_x + \theta_y) =$$
$$\underbrace{U\cos(3\omega t + \theta_x + \theta_y)}_{3\omega\text{-term}} - \underbrace{\frac{1}{2}A_{\dot{x}}\cos(\omega t + \theta_x + \theta_y - \theta)}_{\text{Fundamental cross-flow frequency}} - \underbrace{\frac{1}{2}A_{\dot{x}}\cos(5\omega t + \theta_x + \theta_y + \theta)}_{5\omega\text{-term}}. \tag{11}$$

The global in-line component of the higher harmonic force is written:

$$\dot{y}\cos(3\omega t + \theta_x + \theta_y) =$$
$$A_{\dot{y}}\cos(\omega t)\cos(3\omega t + \theta_x + \theta_y) =$$
$$\underbrace{\frac{1}{2}A_{\dot{y}}\cos(2\omega t + \theta_x + \theta_y)}_{\text{Fundamental in-line frequency}} + \underbrace{\frac{1}{2}A_{\dot{y}}\cos(4\omega t + \theta_x + \theta_y)}_{4\omega\text{-term}}. \tag{12}$$

This idealized example shows that the force model represents frequencies up to the fifth harmonic, for a cylinder that undergoes fundamental frequency vibrations. In time, the cylinder may develop multi-frequency response as a consequence of the loading process. This allows for loads above the fifth harmonic. In theory, all odd and even multiples of ω can be excited, in the cross-flow and in-line directions respectively. Other formulations could have been adopted to provide a similar frequency distribution, e.g. by substituting $\cos(\phi_{\text{exc,y}} + \phi_{\text{exc,x}})$ for $\cos(3\phi_{\text{exc,y}})$ in equation 6. However, higher harmonics is a phenomenon associated with combined motions in cross-flow and in-line directions. If in-line vibrations are eliminated, the $\cos(3\phi_{\text{exc,y}})$-formulations would be unaffected: a property which is unphysical.

2.2.2. Size of higher harmonic load components

A constant force coefficient C_{hh} defines the magnitude of higher harmonic loading in equation 6. Hence, known load dependencies, such as those concerning displacement amplitudes and cylinder trajectories, are disregarded in the present work. Alternatively, amplitude and trajectory dependent load modelling would demand numerical approximations of these parameters continuously in time. The model would then become more complex, computationally slower and less suited to handle time varying flows, such as waves and current combined. The present formulation is only expected to provide an averaged representation of the

higher harmonic fluid loads. However, the claim is that such a simple approach can be useful for response predictions of flexible pipes in current. For instance, the following key features of multi-frequency VIV (see e.g. Wu et al. [7]) should be well represented:

- A tension dominated pipe is more likely to display 3ω vibrations because the eigenfrequencies are more densely packed than for a bending stiffness dominated structure (see section 5).

- For large bandwidth VIV response processes, $d\phi_{\mathrm{exc,x}}/dt$ and $d\phi_{\mathrm{exc,y}}/dt$ are expected to display time variability, which will manifest in their sum frequency $d\phi_{\mathrm{exc,y}}/dt + d\phi_{\mathrm{exc,x}}/dt$. Consequently, less energy is transferred at the higher harmonic eigenfrequencies than if the sum frequency was constant and close to these eigenfrequencies. This is qualitatively in agreement with the experimental findings by Modarres-Sadeghi et al. [9], i.e. that the chaotic response of a riser in current do not contain clear contributions from higher harmonics.

3. Model performance for a two degree of freedom system

Recall that the force model, i.e. equation 1, predicts the hydrodynamic loads on a cylinder strip of unit length. Flexible pipe VIV is modelled by inserting these loads on a finite number of cross-sectional cuts along the structure. The loading at an arbitrary cross-sectional cut is governed by the two-dimensional flow and response characteristics that apply to the same cross-section. Hence, one such cross-sectional cut can be regarded as a two degree of freedom system when axial communication resulting from structural continuity is neglected. In this section, a cylinder that undergoes forced vibrations in two degrees of freedom is analysed to assess whether or not the higher harmonic load term has negative implications for the fundamental frequency predictions. The empirical load parameters that were utilized in this study (ref. table 1) were calibrated for the flexible pipe analysis in section 4. The model is tested with and without the higher harmonic term.

Table 1: Empirical parameters in hydrodynamic force model.

Parameter	Size
C_D	1.2
C_M	2
$C_{v,y}$	0.85
$C_{v,x}$	0.75
$\hat{f}_0$	0.144
$\Delta\hat{f}$	0.064
α	0.15
C_{hh}	0 - 1.5

Dahl [5] conducted experiments with forced cross-flow and in-line harmonic motions of a cylinder in uniform flow. The cylinder was forced to move sinusoidally with displacement time series: $y(t) = A_y \sin(\omega_y t)$ and $x(t) = A_x \sin(\omega_x t + \theta)$. The amplitudes were varied systematically in the ranges $0.25 < A_y/D < 1.5$ and $0 < A_x/D < 0.75$. The relation between phase angel θ and cylinder trajectory is displayed in figure 3. The proposed load model was applied to some of Dahl's test runs for qualitative and (partly) quantitative assessment of its ability to predict the fluid-cylinder power transfer. The average power coefficient C_{ap} was computed from:

$$C_{ap} = \frac{(1/T)\int_T (F_y \dot{y} + F_{x,fluct}\dot{x})dt}{0.5\rho U^3 D}, \tag{13}$$

where T is the simulated time period, F_y is the global cross-flow force per unit length, and $F_{x,fluct}$ is the global in-line load per unit length after subtracting the mean value. The simulations were based on 100 periods of in-line motion, discretised into 400 time steps per in-line period. Properties of the cylinder, its motion, and flow characteristics are provided in table 2.

The average power coefficient is a measure of excitation and damping, and is an important parameter with respect to response amplitudes of VIV. The contour $C_{ap} = 0$ is where the net energy input equals zero. By defining C_{ap} as a time integrated sum of cross-flow and in-line power allows excitation in one degree of

Table 2: Flow and structural characteristics of forced vibration tests [5].

Parameter	Definition	Size
Reduced velocity	$U_r = 2\pi U/(D\omega_y)$	4.5 - 15
Reynolds number	$Re = UD/\nu$	6860 for $U_r \leqslant 6$, else 8760
Diameter	D	0.0381 m
In-line amplitude ratio	A_x/D	0 - 0.75
Cross-flow amplitude ratio	A_y/D	0.25 - 1.5
frequency ratio	ω_x/ω_y	2
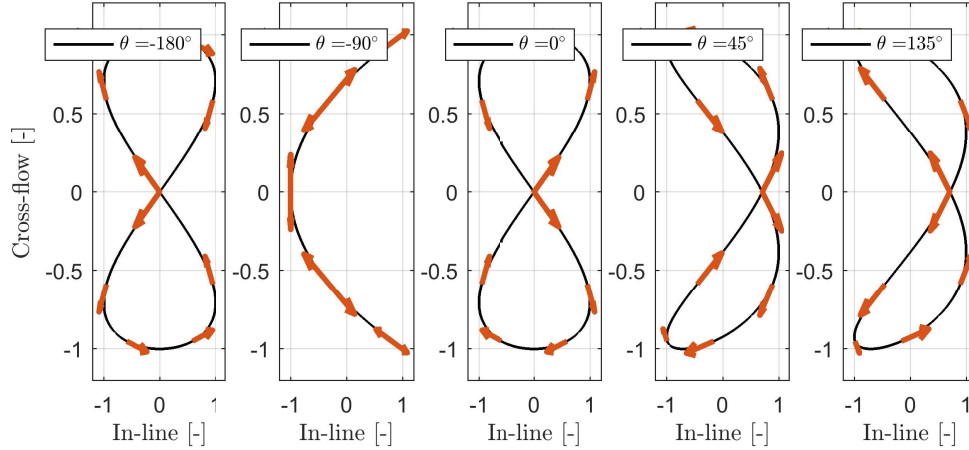
Figure 3: Trajectories for different phase angles

freedom to cancel the damping in the other direction, with a zero net energy transfer. This demonstrates that the surface where $C_{ap} > 0$ may contain both excitation and damping (but where the excitation outweighs the damping). For simplicity, the values of A_x/D and A_y/D where $C_{ap} > 0$ will be referred to as a power-in/excitation region.

Figure 4 displays simulated contours of C_{ap} for three values of reduced velocity. $U_r = 4.5$ is prior to synchronization, 6.5 is within the synchronization band, and 15 is post-synchronization. Both for reduced velocity of 4.5 and 15, the whole domain is controlled by damping forces ($C_{ap} < 0$). For $U_r = 6.5$ the ($C_{ap} > 0$)-region is roughly within $A_x/D < 0.2$ and $A_y/D < 1$, at which vibrations can be excited. By increasing $C_{v,x}$, the ($C_{ap} > 0$)-surface will cover larger in-line amplitudes, and equivalently, a higher value of $C_{v,y}$ will provide excitation for larger cross-flow vibrations. The hydrodynamic damping is governed by Morison's drag force. Thus the drag coefficient is important for the energy transfer. By decreasing C_D, the excitation region will expand towards larger amplitude ratios, and vice versa.

Figure 4 shows contours of C_{ap} for two values of the higher harmonic force coefficient C_{hh}. By increasing this value from 0 to 1.5, a small increase in the average power coefficient is seen. This is due to $\mathbf{F}_{hh}$'s (small) contributions to the fundamental lift and drag forces resulting from the local-global reference transformation (ref. equations 11 and 12). Otherwise, C_{ap} should be independent of the higher harmonic load term, since the prescribed displacement time series do not contain high frequency components. This result suggests that the accuracy of the fundamental response predictions are not significantly affected by the new load term.

Comparisons of C_{ap} from Dahl [5] and simulations are presented in figure 5 for three arbitrary test conditions (in terms of reduced velocity and phase angle). The quantitative agreement is very good considering how many parameters that govern the results (i.e. reduced velocity, Reynolds number, in-line and cross-flow displacement amplitudes, in-line to cross-flow frequency ratio and phase angle), and the simplicity of the proposed model. However, some quantitative discrepancies are evident: The model seems to produce too much excitation for low in-line amplitudes. As the in-line amplitude ratio A_x/D is raised, especially for low values of A_y/D, it seems that the experiments go towards a high damping state at a faster rate than the predictions. These discrepancies could have been reduced by amplitude dependent vortex shedding force co-

efficients; At least for the purpose of providing an accurate representation of the power transfer for cylinders that undergo perfect harmonic vibrations. However, harmonic and stable trajectories are far from the reality of VIV response, especially of flexible pipes. Hence, these discrepancies do not imply that the model is unfit for flexible pipe analysis, which the rest of this paper is devoted to show.
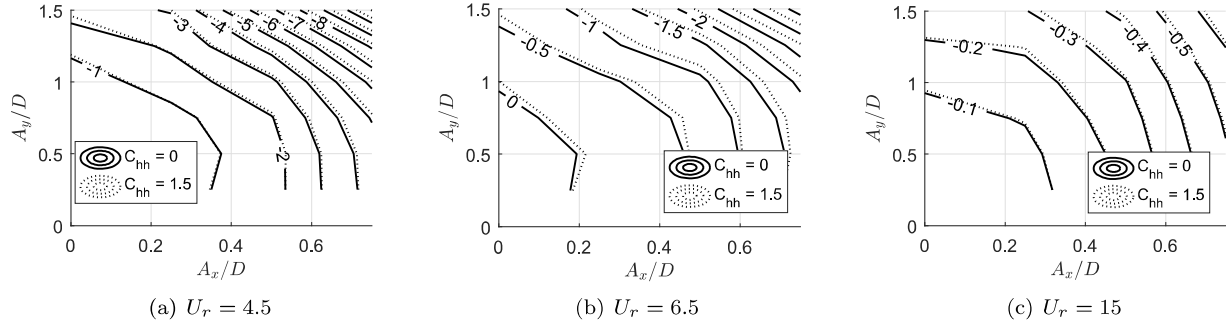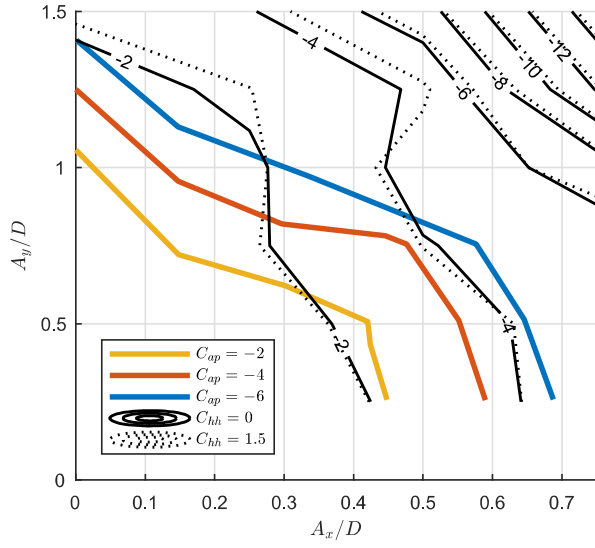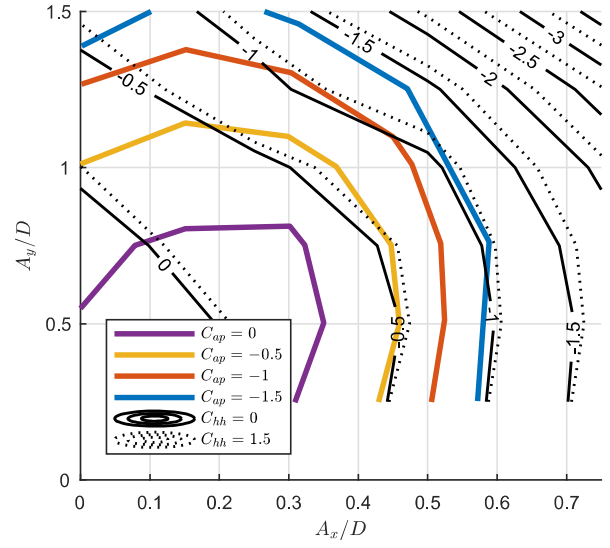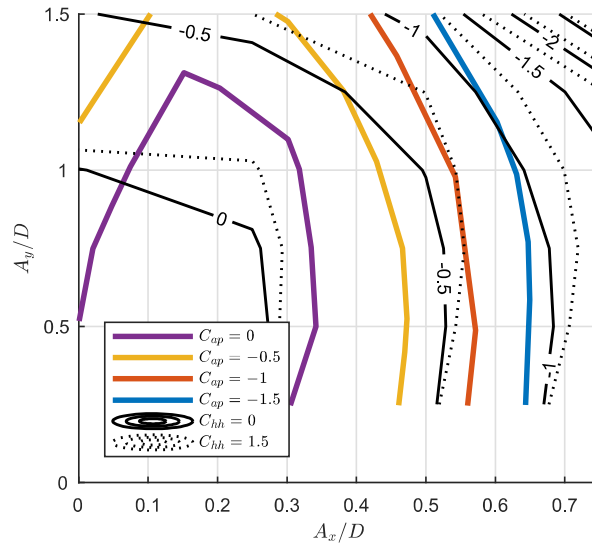

(a) $U_r = 4.5$　　　　　　(b) $U_r = 6.5$　　　　　　(c) $U_r = 15$

Figure 4: Average power coefficient C_{ap} as function of in-line and cross-flow amplitude ratios, for $\theta = 0$.

(a) C_{ap} for $U_r = 4.5$, $\theta = -180°$.

(b) C_{ap} for $U_r = 6.5$, $\theta = 0$.

(c) C_{ap} for $U_r = 7.5$, $\theta = -90°$.

Figure 5: Average power coefficient C_{ap}. Experimental contours by Dahl [5] are included in colours, whereas the simulated results are shown for two values of C_{hh}.

4. VIV of tension dominated riser in uniform current

In this chapter the model is verified against the Norwegian Deepwater Programme Riser High Mode VIV tests [23], which subsequently are referred to as the NDP experiments. Strain measurements of the bare riser configuration in uniform flow are considered, for towing velocities in the range 0.3 m/s to 2.4 m/s. The structural properties of the bare riser are presented in table 3.

Table 3: Structural properties of bare riser in the NDP experiments, uniform flow [23].

Parameter	Size
Length (L)	38 m
Diameter (D)	0.027 m
Bending stiffness (EI)	599 Nm^2
Tension (T)	4067 N - 6285 N
Mass per unit length	0.933 kg/m
Young's modulus (E)	$36.2 \cdot 10^9$ N/m^2

4.1. Numerical and empirical inputs

Response predictions were made by combining the hydrodynamic force model with a linear finite element model. The initial phasing of the vortex shedding forces were randomly distributed along the finite element model, for spatial correlation to build up automatically in time. Beam elements with two rotations and two translations degrees of freedom at each node were used, neglecting pure axial movement and torsion. The elements provide stiffness from bending and tension, where the tension as of table 3, represent the measured tension during each individual test run. 500 such elements were found sufficient with respect to convergence. The response was found by time integration of the dynamic equilibrium equation, by the method of constant average acceleration. 200 time steps per fundamental cross-flow period were used to discretize the time domain, and a total of 450 such periods were simulated. The first 225 were removed prior to post-processing, to make sure no transient effects were included.

Morison's drag and mass coefficient were determined from values commonly employed for stationary cylinders in current, i.e. $C_M = 2.0$ and $C_D = 1.2$. Subsequently, the empirical inputs associated with vortex shedding and higher harmonics were chosen from a visual best fit with cross-flow strain measurements, resulting in a C_{hh} of 1.5. The rest of the coefficients are the same as in the previous section, listed in table 1. The model was also tested without the higher harmonic term, but with otherwise the same parameters.

4.2. Filtering

Before the simulations are experimentally validated it is to be noted that all the VIV response signals have been band-pass filtered. This operation has been performed to distinguish between the fundamental responses (at 1ω and 2ω in the cross-flow and in-line directions respectively), and the total/"unfiltered" signals. The results are summarized in table 4. The Fourier Transform of the experimental time series were plotted to manually identify the frequency ranges associated with the fundamental and higher harmonic responses, and to find the peak frequencies: ω and 2ω. The simulations were treated in a similar fashion to determine appropriate frequency bandwidths. However, since the simulations are considered to be "noise-free" whereas the experiments contain noise, there are some differences in the limits that were applied.

Table 4: Frequency bandwidths for NDP experiments and simulations. Abbreviations: CF - Cross-flow, IL - In-line.

	Experiment	Simulation
CF 1ω	0.75 Hz - 2ω	0 Hz - 2ω
IL 2ω	1.5 Hz - 3ω	$\approx 1\omega$ - 3ω
CF	0.75 Hz - 6ω	unlimited
IL	1.5 Hz - 12ω	$\approx 1\omega$ - unlimited

4.3. General trends

Figure 6 shows results obtained from time domain simulations using $C_{hh} = 0$, accompanied by the experimental counterparts. The left plot presents space averaged values of root mean square (rms) of cross-flow strains, as function of current velocity. The labels: "Sim" and "Exp" represent the unfiltered values from simulations and experiments respectively, whereas the extension "1ω" denotes the bandpass-filtered results including frequencies in range of the fundamental frequency. The relationship between the fundamental frequency and current velocity is shown in the right plot.

The strain comparison demonstrates that the fundamental predictions are accurate. However, the higher order strain contributions are too small to reach the unfiltered experimental strain levels. The latter suggests that the additional higher harmonic load term can be useful to amplify the higher harmonic components. The dominating frequencies compare well, which indicates that the structural model and the cross-flow synchronization (i.e. $\hat{f}_0$ and $\Delta\hat{f}$) are well defined.
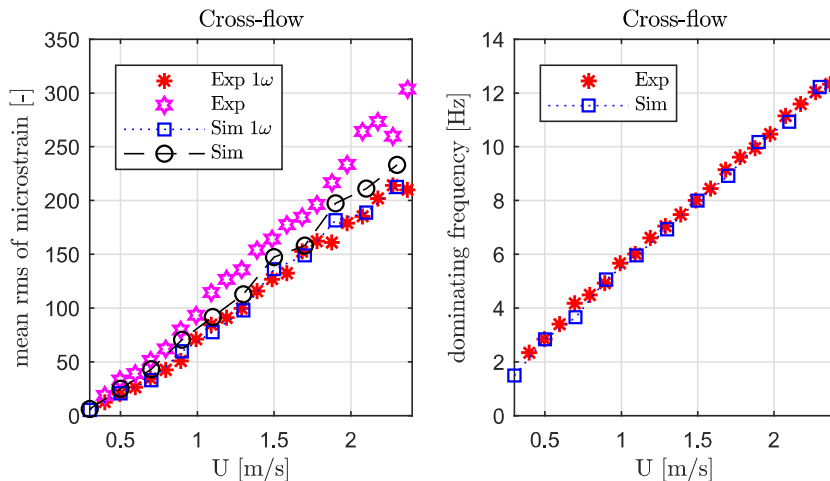
Figure 6: Mean root mean square (rms) of strain and dominating frequency for current velocities 0.3-2.4 m/s. The results are obtained from simulations with $C_{hh} = 0$. Experimental case: NDP.

The rest of this chapter is devoted to the case of $C_{hh} = 1.5$, with special emphasis on validating the higher harmonic response predictions against the experimental data. Prior to this the fundamental frequencies in the cross-flow and in-line directions are presented in figure 7, to confirm that the new loading term does not change the cross-flow synchronization, and to demonstrate that the in-line synchronization, with $\alpha = 0.15$, comply with the 2ω-relationship. The figure confirms that both these aspects are satisfied, and the experimental agreement is seen to be very good.

The mean value of rms of cross-flow and in-line strains are plotted in figure 8 (a). As opposed to figure 6, the outputs from simulations include envelops (as shaded regions) of minimum and maximum strain level, for each current velocity. These values were obtained from dividing the whole time series (consisting of 225 cross-flow VIV periods) into five equally long time windows (of 45 periods each). Subsequently, the five time series were post-processed independently, where the mean value, over the whole time series, was represented by dotted/stippled lines with markers. By including these envelops one can detect if the response process reach steady-state, at which the minimum, maximum and mean values should coincide. The figure indicates that the strain signal is steady-state for velocities less than 1 m/s, but from there displays increasing variability for increasing current speed. This is in qualitative agreement with several high mode VIV experiments at which the response becomes stochastic and hence undergoes large variations [8, 24, 25]. Furthermore, both the filtered and unfiltered cross-flow strain signals show improved correlation with the NDP measurements relative to the $C_{hh} = 0$ case. This confirms that the additional load term serves its purpose of amplifying the higher harmonic responses, and that the fundamental predictions remain accurate. It is to be noted that the in-line strain does not fit the measurements with same level of accuracy as the cross-flow counterpart, and that the higher harmonic load term to a less extent induce higher harmonic in-line vibrations. However, the experimental results clearly show that the higher harmonic in-line response is small relative to the fundamental component (at 2ω), which supports the decision to apply $\mathbf{F}_{hh}$ in the local cross-flow direction.

The ratios of mean rms of strain from fundamental and total response $\epsilon_{1\omega}/\epsilon$ are given in figure 8 (b), and supports the above discussion.
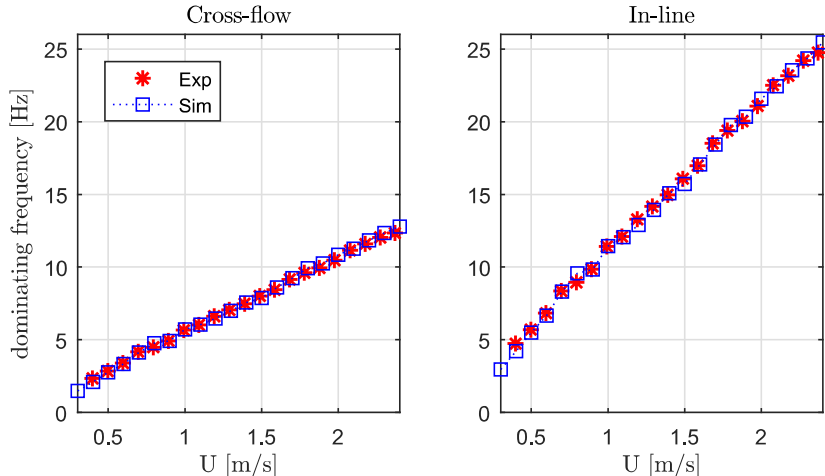

Figure 7: Dominating frequency for current velocities 0.3-2.4 m/s. Experimental case: NDP.

VIV in general, and higher harmonics in particular, are of practical interest due to fatigue damage of slender structures. Therefore, the time series of strain have been post-processed to assess the model with respect to fatigue, in cross-flow and in-line directions separately. First, the axial bending stresses were computed from a linear stress-strain relationship. Subsequently, stress ranges were identified by rainflow counting in the WAFO toolbox [26]. An SN-curve for non-welded pipe sections without corrosion protection [27] was used to relate number of cycles until failure (N) with the stress ranges (S): $\log N = 12.436 - 3 \log S$. The Miner-Palmgren's law was then utilized to calculate the accumulated fatigue damage, by summing up the damage for each stress range. The maximum damage along the riser was identified for each velocity, and the result is presented in figure 9.

Figure 9 (a) shows that the fundamental damage in the cross-flow direction is accurately predicted by the model. The total damage is also well represented, but the model tends to produce non-conservative outputs for velocities above 1.8 m/s. However, at $U = 2.3$ m/s the fit is accurate, which suggests that the experimental counterpart becomes increasingly scattered for the highest flow cases, probably because of the inherent stochastic nature of high mode VIV. The experimental agreement could have been improved by a slight increase of C_{hh} towards the highest velocities. It should be noted that the SN-curve that was adopted in this study is inverse proportional to the cube of the stress range. Consequently, small discrepancies in the original strain time series might lead to large discrepancies in the fatigue plot. As for the strain signals, the in-line fatigue predictions provide a rough approximation to the experimental data. To give a clear indication on the importance of higher harmonics, the ratios of maximum fatigue at the fundamental frequencies $\bar{D}_{1\omega}$, over the total damage $\bar{D}$, are given in figure 9 (b). The latter shows that the cross-flow damage is amplified by a factor of approximately 2.5 to 10, when higher harmonics are accounted for.
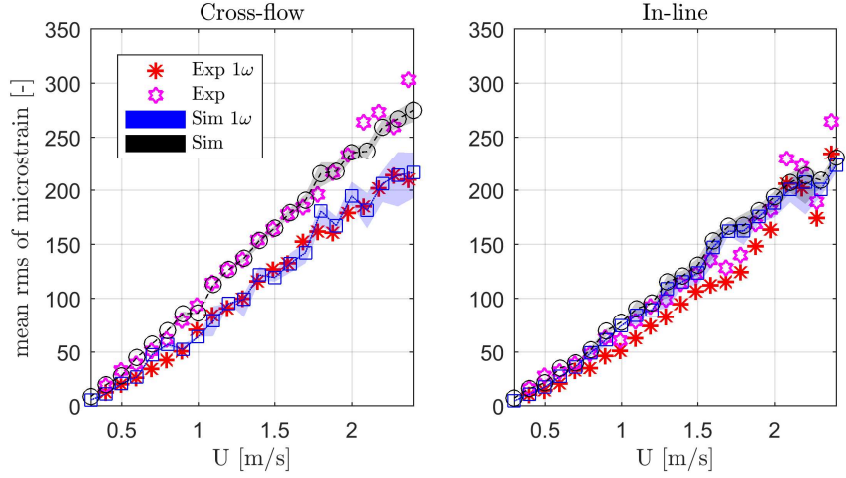
(a) Mean rms of strain
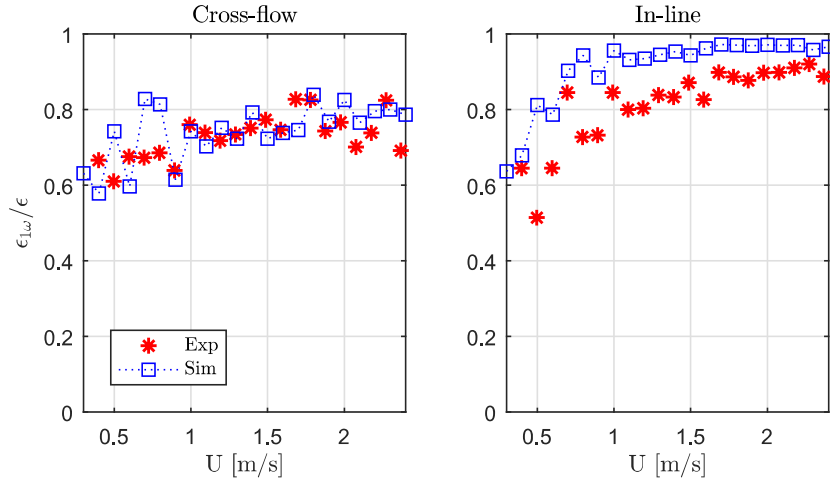
(b) Ratio of mean rms of strain

Figure 8: Mean of root mean square (rms) of strain along the riser for current velocities 0.3-2.4 m/s. Shaded areas contain minimum and maximum values obtained from splitting the whole time series into five equally long time windows, where each of the windows were post-processed independently. The dotted/stippled lines with markers represent the mean value over the whole time series. Experimental case: NDP.
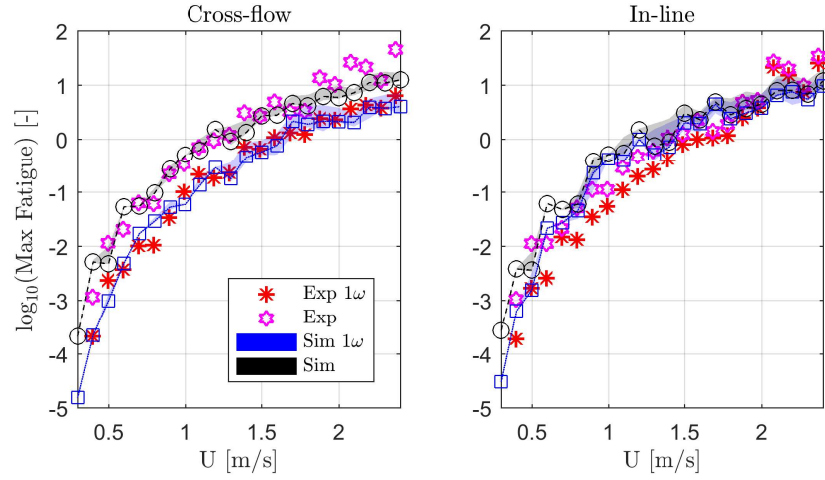
(a) Maximum riser fatigue
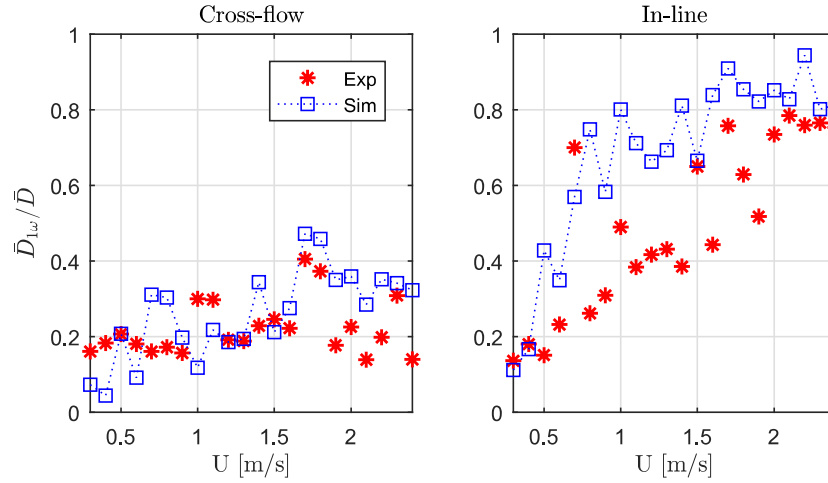
(b) Ratio of average maxium fatigue damge

Figure 9: Maximum fatigue for current velocities 0.3-2.4 m/s. Shaded areas contain minimum and maximum values obtained from splitting the whole time series into five equally long time windows, where each of the windows were post-processed independently. The dotted/stippled lines with markers represent the mean value over the whole time series. Experimental case: NDP.

4.4. Cross-flow response details

To give an in-depth examination of the cross-flow response predictions and how they agree with measurements, figure 10-12 are included. The former addresses the actual strain time series, at the position of maximum rms value, for three current velocities. The associated frequency components, and how they develop in time, are shown in terms of wavelet plots. Results from simulations (Sim) are accompanied by the experimental output (Exp). Two main findings are extracted from figure 10: Firstly, Both ω and 3ω match the measurements in terms of value and partly in terms of strength. This illustrates that the frequency distribution at which the load model transfers energy to the structure is well represented (ref. section 2.2.1). In addition, despite having constant load coefficients, the amount of energy that is transferred at these frequencies is of sufficient accuracy for the experimental and simulated strain amplitudes to display quantitative agreement. Secondly, the predicted response process appears irregular in time for the moderate and high velocity cases in (b) and (c), with frequency variations and amplitude modulations that does not repeat periodically. This feature is in qualitative agreement with the experimental counterparts, although the latter seem to undergo slightly more amplitude modulations. Since irregular response seems to be a model feature that only applies to the high flow velocity cases, it might correlate with the response mode. For high mode vibrations, the relative distances between the neighbouring eigenfrequencies reduce, under which the synchronization range (given by $\hat{f}_0$ and $\Delta\hat{f}$) will include several eigenfrequencies. This might result in an unstable synchronization process, where the cross-flow vortex shedding load is unable to reach stable synchronization with only one eigenfrequency. The effects associated with the relative velocity (e.g. the local-global reference frame transformation in section 2.2.1) might also contribute to the response variability produced by the model.

Response variability is also addressed in figure 11, by presenting the dominating fundamental cross-flow response frequency, and how it varies along the riser (z/L) and in time (t). Although the experimental agreement looks poor by a direct visual comparison, this is not the case if one accept the plots as realizations of random processes. The proposed load formulation is indeed deterministic, however the initial phasing of vortex shedding is randomly distributed along the rise. Consequently, for the high velocity cases where the response appear to be irregular, a new frequency composition will display from a new simulation with different initial conditions. The point of including figure 11 is to demonstrate that the experimental and simulated strain signals are of similar frequency bandwidth, and that both time and space variability occurs. The distinct transitions between dominating frequencies seen in the experimental datasets might simply result from the coarse mesh between the longitudinal measuring stations.

The axial distribution of fatigue damage is presented in figure 12. It demonstrates that fundamental and total damage are of same order of magnitude as the measurements. The spatial distributions are not completely accurate, but provide very good estimates for all practical purposes. However, in figure 12 (c), the position of maximum fatigue measured is near the opposite end to that from simulation. Why this discrepancy is non-critical is explained as follows:

The NDP experiment is modelled in a symmetric fashion, i.e. pinned boundaries at both ends of the riser, exposed to a uniform current profile. Despite the structural and flow symmetries, the VIV response tends to develop in a non-symmetric fashion for high flow velocities, more strongly near one of the riser's ends. This is seen for both the experiment and simulation in figure 12 (b) and (c). The vortex shedding loads are initiated with a random phasing, and there are no structural or flow asymmetries that drives the response towards one specific riser end. The consequence is that there is an equal probability that the critical location appears left or right on the riser. In reality, there are always some asymmetries in the experimental set-up that will favour the response to develop largest amplitudes towards a specific end.
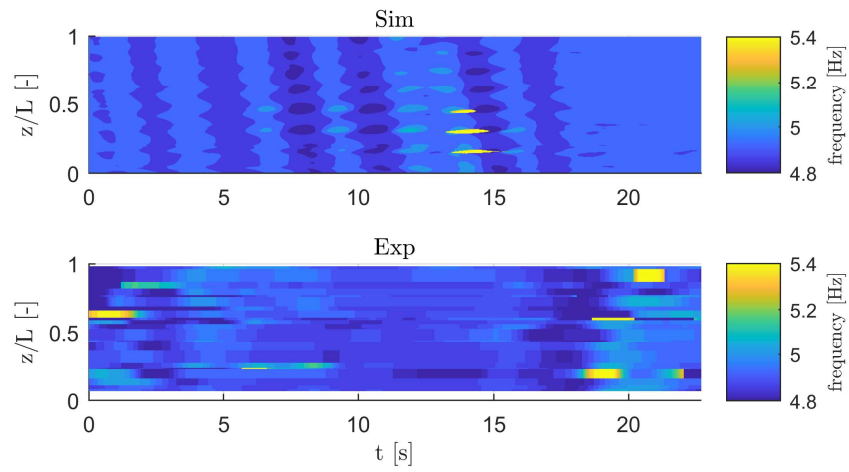
16
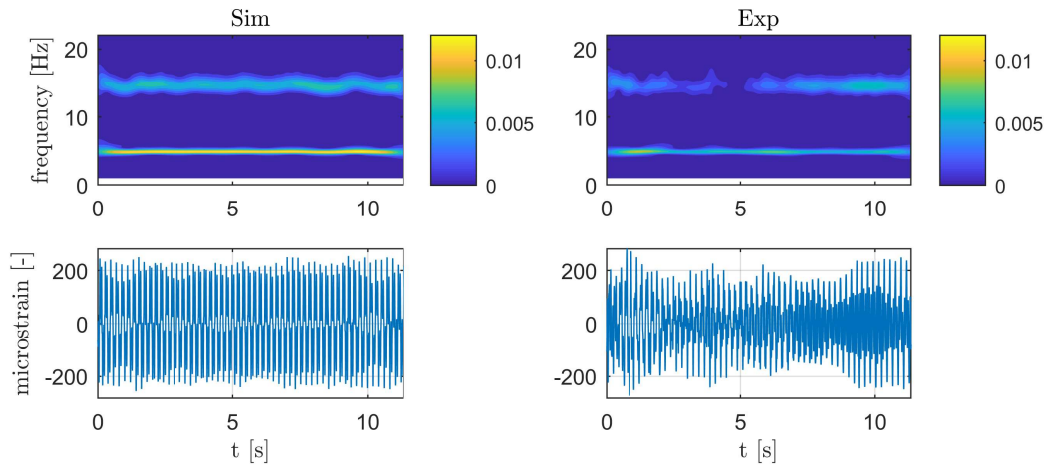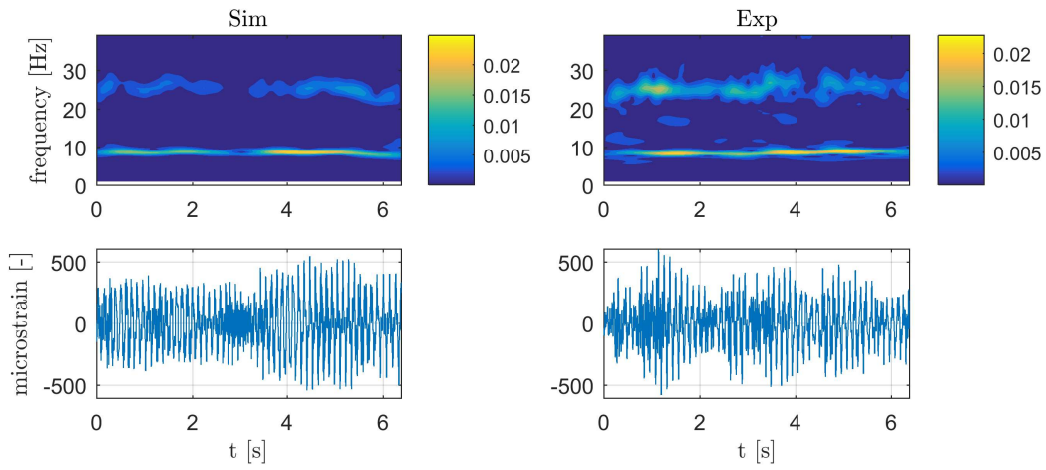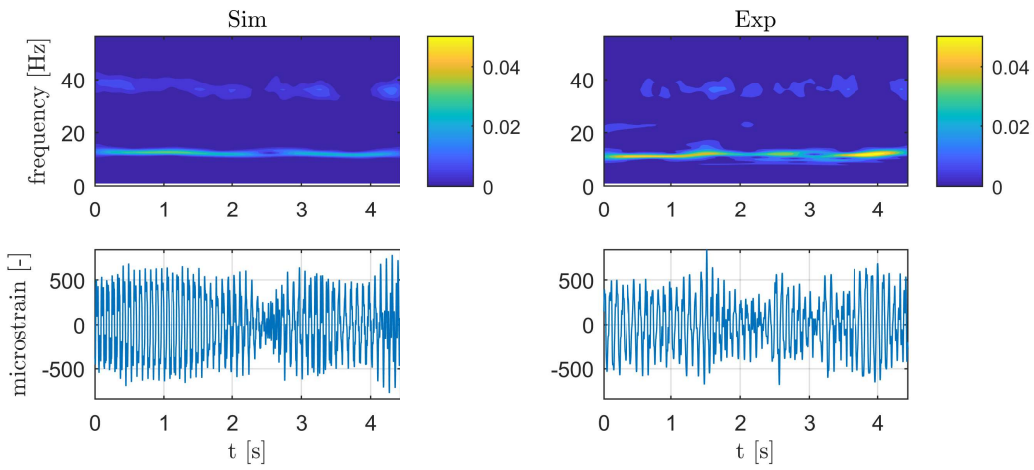
(a) U = 0.9 m/s

(b) U = 1.6 m/s
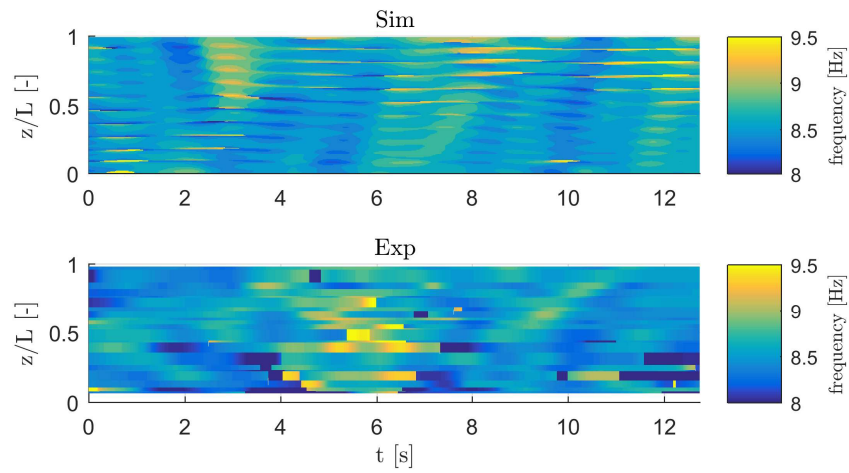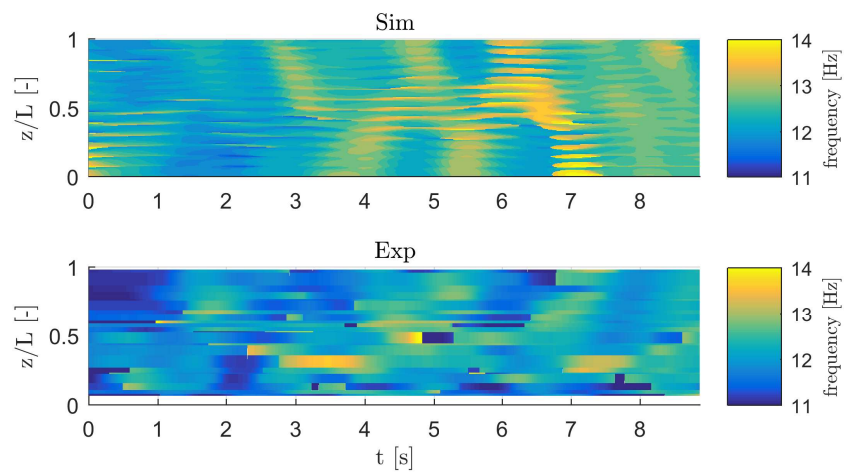

(c) U = 2.3 m/s

Figure 10: Wavelet frequency plot and corresponding strain signal at position with maximum rot mean square (rms) of strain. Experimental case: NDP.
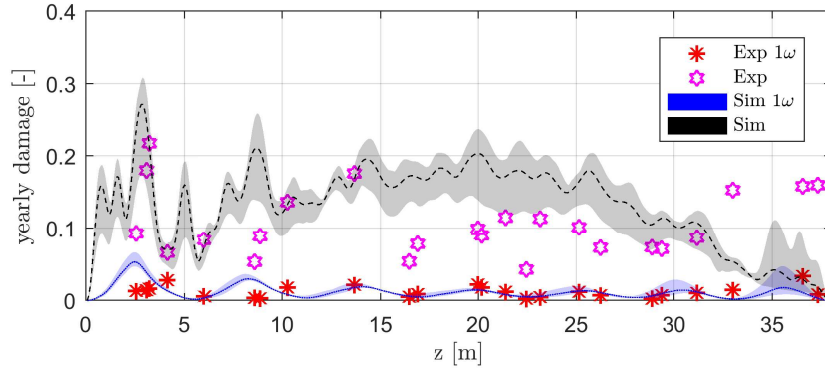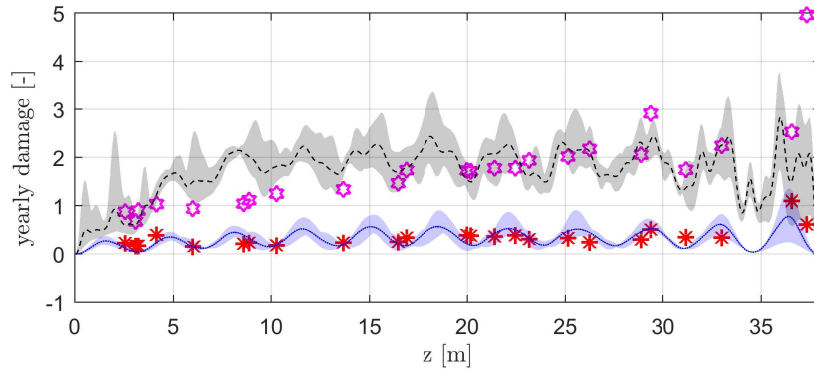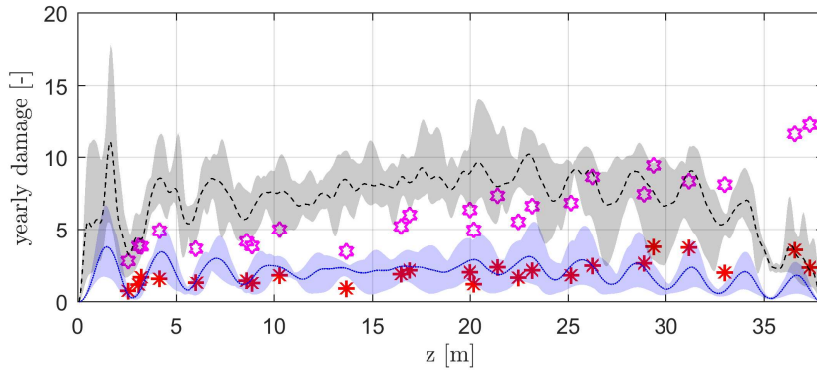
(a) U = 0.9 m/s

(b) U = 1.6 m/s

(c) U = 2.3 m/s

Figure 11: Axial and time distribution of dominating (fundamental) frequency. Experimental case: NDP.

(a) U = 0.9 m/s

(b) U = 1.6 m/s

(c) U = 2.3 m/s

Figure 12: Axial distribution of fatigue damage. Shaded areas contain minimum and maximum values obtained from splitting the whole time series into five equally long time windows, where each of the windows were post-processed independently. The dotted/stippled lines represent the mean value over the whole time series. Experimental case: NDP.

5. Verification

Section 4 demonstrated the potential of the proposed VIV prediction tool. However, the coefficients were chosen to give a best fit with respect to the strain measurements. Hence, it is fair to question the generality of this particular choice of $C_{v,x}$, $C_{v,y}$ and C_{hh}. To validate the robustness of the method and the choice of empirical coefficients, three additional flexible pipe experiments in uniform flow have been simulated, assuming C_{hh}, $C_{v,x}$ and $C_{v,y}$ to be the same as in the previous section (for $C_{hh} = 1.5$). Results for modified sets of parameters are also included, to address the response sensitivity. The experiments cover a range from tension to bending stiffness dominated cases. This allows us to study how the structural properties affect the higher harmonic response contribution, and to what extent the proposed model is able to reflect these findings. To provide a quantitative measure of the degree of tension/beam dominated system, a parameter Ω_n is introduced:

$$\Omega_n = \frac{\omega_{s,n}{}^2}{\omega_{b,n}{}^2}. \tag{14}$$

$\omega_{s,n}$ and $\omega_{b,n}$ are the angular eigenfrequencies of a tensioned string and a hinged-hinged untensioned beam, respectively:

$$\omega_{s,n} = \frac{n\pi}{L}\sqrt{\frac{T}{m}}$$
$$\omega_{b,n} = (\frac{n\pi}{L})^2\sqrt{\frac{EI}{m}}. \tag{15}$$

n is here the (cross-flow) mode of vibration and m is taken to be the sum of structural mass and still water added mass, per unit length. We expect that the larger Ω_n becomes, the more the flexible pipe will behave like a tensioned string, and the more the response will be influenced by 3ω. The latter results from the fact that string eigenfrequencies are a linear function n, as oppose to a n^2 relationship for untensioned beams. Table 5 contains values of Ω_n for the three additional experimental case studies. For comparison, the same parameter was computed for the NDP simulations and the result is presented in figure 13. Information on flow and structural properties is provided in table 6. For further details see Vandiver et al. [2], Soni [28] and Huse [29], for Lake Seneca, NTNU and Ormen Lange experiments respectively.

To predict VIV, linear finite element models of straight pipes have been combined with the hydrodynamic load model in equation 1, in a similar manner as for the NDP case (ref. section 4.1). The experimental set up of the Lake Seneca riser gave a small inclination angle at the top end. The latter was simulated by reducing the current velocity in the upper pipe region according to the values provided by Vandiver et al. [2] (i.e. from 0.54 m/s at the top to 0.61 m/s in the lower end). The pipe tension for the NTNU and Ormen Lange simulations was taken as the mean experimental value under steady-state VIV, hence accounting for an increase of geometric stiffness produced by the drag deflection. Numerical inputs are presented in table 7, and the empirical coefficients are the same as for the NDP case (if not stated otherwise).

Table 5: Dominating structural behaviour.

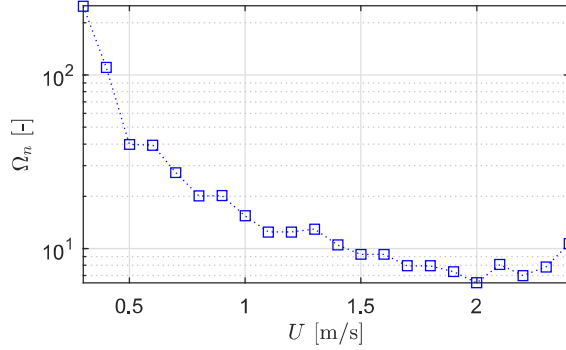| Experiment	CF mode (n)	Ω_n	Structural behaviour
Lake Seneca	17	41.61	String
NTNU	4	0.63	Beam
Ormen Lange	3	0.52	Beam

Figure 13: Dominating structural behaviour from NDP simulations.

Table 6: Flow and structural properties for the additional flexible pipe experiments.

Parameter	Lake Seneca	NTNU	Ormen Lange
Current velocity	0.54 m/s - 0.61 m/s	0.45 m/s	0.23 m/s
Length	122.23 m	10.05 m	11.4 m
Diameter	0.0333 m	0.02 m	0.0326 m
Dry mass	1.176 kg/m	0.499 kg/m	1.147 kg/m
Top Tension	3591 N	88.5 N	72 N
Bottom Tension	3225 N	88.5 N	72 N
Bending stiffness	429 Nm^2	90.1 Nm^2	201 Nm^2
Structural damping ratio	-	1.3 %	0.4 %

Table 7: Numerical inputs used in simulation.

Parameter	Lake Seneca	NTNU	Ormen Lange
Number of elements (ne)	800	200	150
Number of elements per CF dominating mode (ne/n)	47	50	50
Approx. number of time steps per CF period	300	300	300
Number of CF periods in steady-state range	250	250	250

5.1. Lake Seneca

The power spectral density (PSD) of acceleration measurements for the Lake Seneca experiment is presented in figure 14 (a) and (b), at a position in the upper and lower halves of the riser respectively. Below the experimental PSDs, the results from simulations are plotted, at the same axial positions. The original empirical inputs were tested in (c) and (d), and results obtained from analysis with $C_{hh} = 1.2$ are shown in (e) and (f). Qualitatively, the predictions appear highly realistic. The frequency bandwidths, and which of the higher harmonic frequencies that contribute to the total response, fit the measurements quite closely, both in the cross-flow (blue) and the in-line (red) directions. The fundamental cross-flow frequency ω is slightly lower in the simulations, and this difference amplifies for the higher harmonic components because they are multiples of ω. For better experimental agreement, the synchronization range could have been shifted towards higher non-dimensional frequencies to obtain resonance at higher mode numbers. However this operation would also have resulted in higher peaks in the PSDs. It is difficult to quantitatively assess power spectral densities because their visual appearance is very sensitive to how densely the data points are distributed along the frequency axis. Despite of this, it appears that the model induces too much 3ω response. As expected, the higher harmonics are reduced when $C_{hh} = 1.2$, which results in better experimental agreement. The Lake Seneca riser was highly tensioned dominated (ref. table 5), and so was the NDP experiments at low velocities (ref. figure 13). For the latter case, the ratio of fundamental to total cross-flow damage in figure 9 (b) was on average too low for $U < 0.7$ m/s. These findings might suggest that a C_{hh} less than 1.5 provides more accurate predictions for tensioned dominated structural behaviour. However, it should be noted that parts of the discrepancies in figure 14 might be attributed to the simplified structural model (as the real life riser had an initial top angle), and how the current velocity distributes in the axial direction.

(a) Experiment [2]   (b) Experiment [2]

(c) $C_{hh} = 1.5$ (d) $C_{hh} = 1.5$

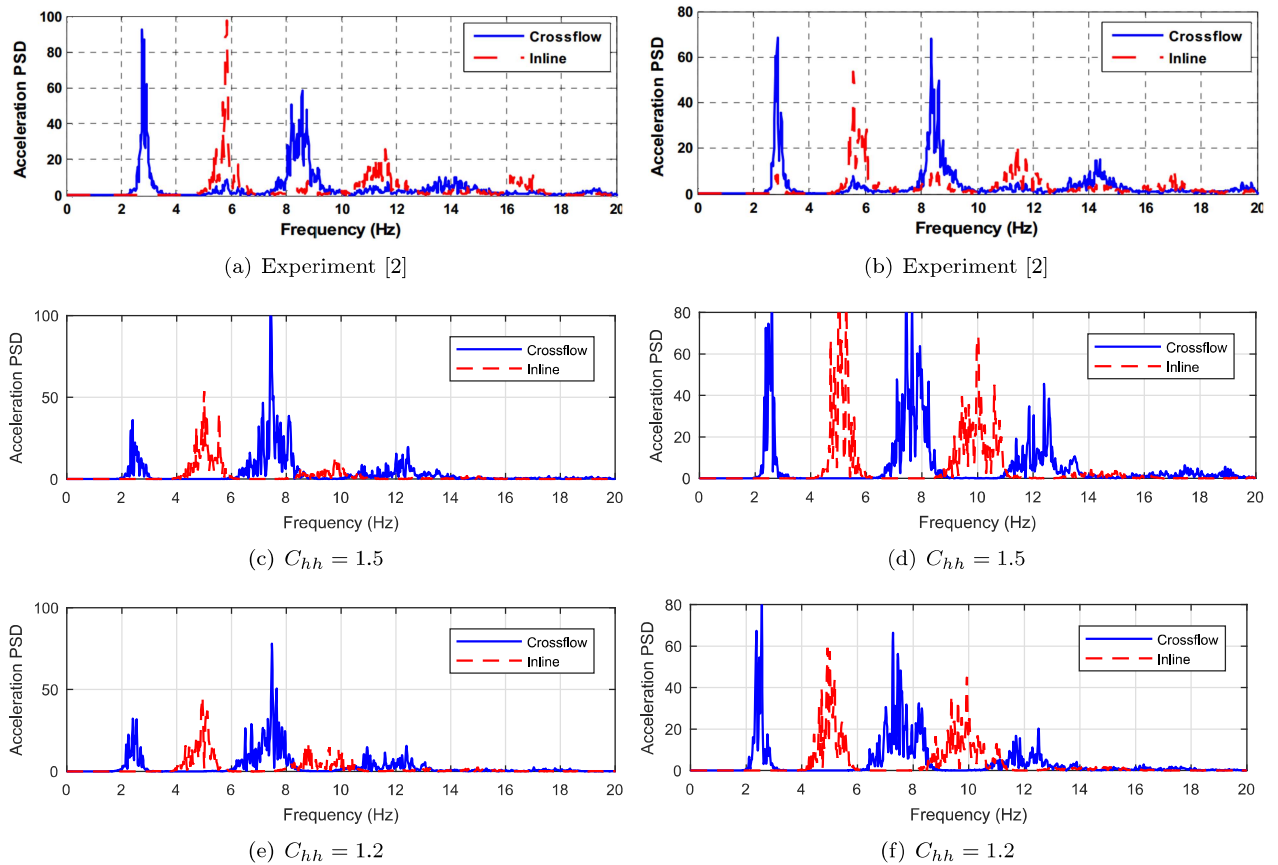(e) $C_{hh} = 1.2$ (f) $C_{hh} = 1.2$

Figure 14: Power spectral density of structural acceleration at two location along the riser. Left: At an axial position 19 % of total length from the top end. Right: At an axial position 77 % of total length from the top end. Experimental case: Lake Seneca.

5.2. NTNU

The longitudinal distribution of cross-flow acceleration rms is extracted from two experimental test runs by Soni [28], at the same towing velocity. This, together with the model predictions, are shown in figure 15, for (a) original choice of empirical input and (b) alternative coefficients. Comparing the experimental results exemplifies the variability and stochastic nature of VIV, as the two test runs show differences. Nevertheless, predictions with the original parameters reflect the measurements in a satisfactory way, but appear slightly conservative (ref. (a)). Reducing $C_{v,y}$ from 0.85 to 0.65 (keeping all other coefficients constant) provides a better fit for the experiment labelled with circles (ref. (b)).
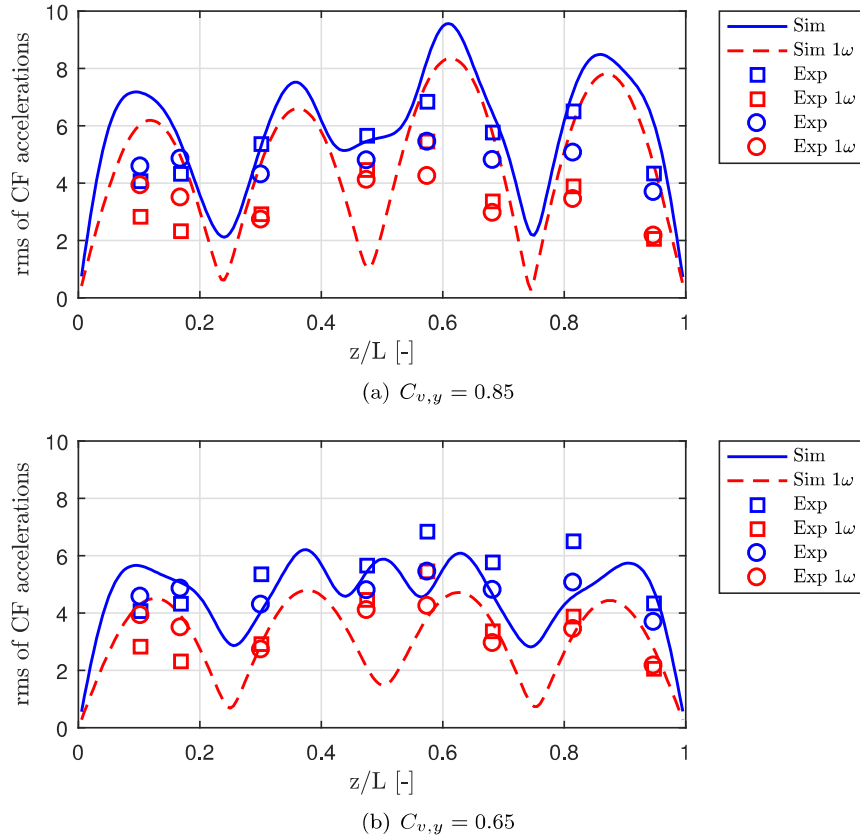

(a) $C_{v,y} = 0.85$

(b) $C_{v,y} = 0.65$

Figure 15: Longitudinal distribution of cross-flow acceleration root mean square (rms). Experimental case: NTNU.

5.3. Ormen Lange

The most bending stiffness dominated case considered is the Ormen Lange experiment (test series 10) [29]. Strain gauges were used to measure the response, and its rms distribution along the pipeline is presented in figure 16, together with the model predictions. The result is highly interesting because it shows that the response is completely dominated by the fundamental frequency. From an experimental standpoint this is not very surprising for a bending stiffness dominated structure. However, a significant finding is that also the model produces nearly pure fundamental frequency response, despite $C_{hh} = 1.5$. This might be surprising because the load model does not know anything about the bending stiffness, and will consequently contain higher harmonic components of same order of magnitude as for a tensioned dominated riser. This is demonstrated in figure 17 which in fact shows that the 3ω lift force (at ≈ 3.75 Hz) exceeds the fundamental component (at ≈ 1.25 Hz) for the Ormen Lange simulation. Some interesting implications can be extracted from this finding. Firstly, it suggests that the higher harmonic VIV response process to a large extent is driven by the structural characteristics of the pipe, and that the magnitude of the higher harmonic loading is of less significance for low values of Ω_n (ref. equation 14 and table 5). Secondly, the finding indicates that the

higher harmonic load term $\mathbf{F}_{hh}$ can be included in VIV analysis of bending stiffness dominated structures, in addition to tension dominated ones.

The original choice of empirical coefficients overestimates the vibration amplitudes. In order to provide a better experimental fit, $C_{v,y}$ had to be reduced from 0.85 to 0.65. C_{hh} was kept at 1.5. The updated predictions are labelled "Sim mod" and "Sim mod 1ω", in figure 16 respectively.
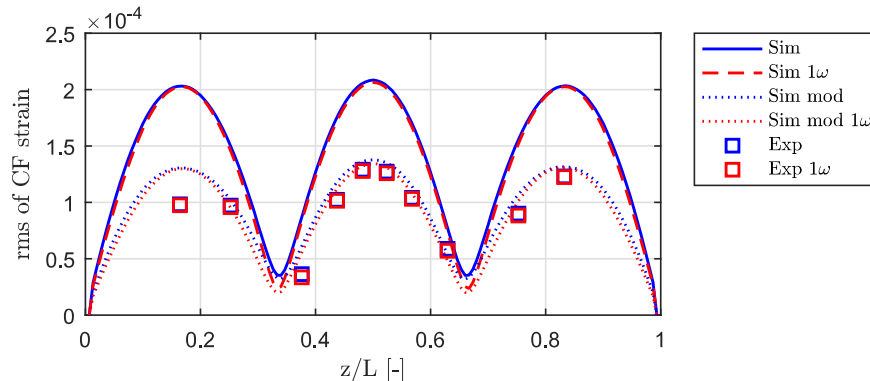

Figure 16: Longitudinal distribution of cross-flow strain root mean square (rms). Experimental case: Ormen Lange.
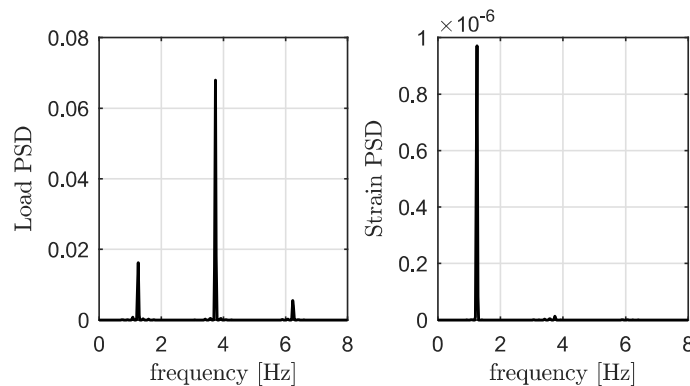

Figure 17: Power spectral density from numerical simulation of cross-flow load and strain at the mid-location of the pipeline. The results were obtained from simulation with the coefficients in table 1 and $C_{hh} = 1.5$. Experimental case: Ormen Lange.

5.4. Reynolds number

The fluid dynamics around a cylinder in current is known to depend strongly on Reynolds number (Re) [30]. For the Ormen Lange experiment Re was about 7500 and for NTNU about 9000. Recall that the original choice of empirical parameters were chosen for best fit with the NDP measurements at Re in the interval 8000 to 65000. Swithenbank et al. [31] looked at the amplitude of cross-flow vibrations for a variety of flexible pipe experiments, and found that they in general were increasing as Re was raised. The latter was also considered by Thorsen et al. [18] who suggested that $C_{v,y}$ is a monotonic function of Reynolds number. Hence, it might be reasonable that the optimal cross-flow vortex shedding force coefficient was lower for the two pipeline cases, than for NDP (i.e. 0.65 versus 0.85). However, a larger database of measurements should be analysed to provide more reliable estimates of optimal empirical coefficients, and to map their Re-dependency.

6. Conclusion

A previously published hydrodynamic load model for VIV predictions in time domain, has been updated. The new feature is a term which controls the magnitude of higher harmonic lift (and partly drag) forces, through an additional empirical coefficient C_{hh}. The fluid-structure energy transfer was studied for cylinder

strips that underwent forced vibrations. It was demonstrated that the (fundamental) energy transfer was just moderately affected by the new higher harmonic term.

The new model was subsequently tested on an experimental case of a tensioned dominated riser towed with constant speed, using linear finite elements. The empirical coefficients were chosen to optimize the cross-flow strain predictions over a range of current velocities. It was shown that, without the higher harmonic term, only the fundamental frequency VIV was predicted. However, by introducing the higher harmoinc term in the load formulation, with $C_{hh} = 1.5$, VIV was estimated with a high level of accuracy, both in terms of strain, fatigue, frequency, response variability and higher harmonics. Furthermore, vortex-induced vibrations of three additional elastic pipe experiments in constant current were simulated. These included one tension dominated riser and two bending stiffness controlled pipelines. The proposed hydrodynamic force model was, together with linear structural models, able to provide reasonable estimates of VIV for the same choice of empirical coefficients. The model performance for an alternative set of coefficients was also included to illustrate response sensitivity with respect to $C_{v,y}$ and C_{hh}. A key finding was that the Ormen Lange experiment (i.e. the most bending stiffness dominated case) was more or less unaffected by higher harmonics, and that the model was able to replicate this feature even though C_{hh} was kept at 1.5. The latter strengthens the belief that the proposed load model can be applied to simulate fundamental and higher harmonic VIV of flexible pipes for a range structural conditions, and that the distance between each eigenfrequency is a main driving factor for the occurrence of higher harmonic response of such structures.

For future work, an extensive amount of experimental data should be analysed in order to optimize the empirical coefficients with more certainty, and provide probabilistic distributions of their values. Higher harmonics of slender structures facing flow profiles other than uniform should also be addressed.

7. Acknowledgement

8. References

[1] J. K. Vandiver, T. Y. Chung, Predicted and measured response of flexible cylinders in sheared flow, in: ASME Winter Annual Meeting Symposium on Flow-Induced Vibration, 1988.

[2] J. K. Vandiver, V. Jaiswal, S. B. Swithenbank, V. Jhingran, Fatigue damage from high mode number vortex-induced vibration, in: Proceedings of the International Conference on Offshore Mechanics and Arctic Engineering - OMAE, 2006.

[3] J. K. Vandiver, V. Jaiswal, V. Jhingran, Insights on vortex-induced, traveling waves on long risers, Journal of Fluids and Structures 25 (4) (2009) 641–653.

[4] N. Jauvtis, C. H. K. Williamson, The effect of two degrees of freedom on vortex-induced vibration at low mass and damping, Journal of Fluid Mechanics 509 (2004) (2004) 23–62.

[5] J. Dahl, Vortex-Induced Vibration of a Circular Cylinder with Combined In-line and Cross-flow Motion, Ph.D. thesis, Massachusetts Institute of Technology, 2008.

[6] J. Wu, D. Yin, H. Lie, C. Larsen, R. Baarholm, V. Jhingran, S. Liapis, On the occurrence of higher harmonics in the VIV response, in: Proceedings of the International Conference on Offshore Mechanics and Arctic Engineering - OMAE, 2015.

[7] J. Wu, D. Yin, H. Lie, C. M. Larsen, R. Baarholm, S. Liapis, On the significance of the higher order stress in riser VIV response, Under review at Journal of Offshore Mechanics and Arctic Engineering .

[8] H. Lie, C. M. Larsen, K. E. Kaasen, Frequency Domain Model for Prediction of Stochastic Vortex Induced Vibrations for Deep Water Risers, in: Proceedings of the ASME 27th International Conference on Offshore Mechanics and Arctic Engineering, 2008.

[9] Y. Modarres-Sadeghi, F. Chasparis, M. Triantafyllou, M. Tognarelli, P. Beynet, Chaotic response is a generic feature of vortex-induced vibrations of flexible risers, Journal of Sound and Vibration 330 (11) (2011) 2565–2579.

[10] E. Passano, C. M. Larsen, H. Lie, J. Wu, Vivana Theory Manual, Tech. Rep., 2014.

[11] J. K. Vandiver, L. Li, SHEAR7 V4.4 Program Theoretical Manual, Tech. Rep., Department of Ocean Engineering Massachusetts Institute of Technology, 2005.

[12] DNV GL, Recommended Practice DNV-RP-F204 Riser Fatigue, Tech. Rep., 2010.

[13] X. Q. Wang, R. M. C. So, K. T. Chan, A non-linear fluid force model for vortex-induced vibration of an elastic cylinder, Journal of Sound and Vibration 260 (2) (2003) 287–305.

[14] H. Zanganeh, N. Srinil, Three-dimensional VIV prediction model for a long flexible cylinder with axial dynamics and mean drag magnifications, Journal of Fluids and Structures 66 (2016) 127–146.

[15] V. Jhingran, J. K. Vandiver, Incorporating the Higher Harmonics in VIV Fatigue Predictions, in: Proceedings of the 26th International Conference on Offshore Mechanics and Arctic Engineering, 2007.

[16] Y. Modarres-Sadeghi, H. Mukundan, J. Dahl, F. Hover, M. Triantafyllou, The effect of higher harmonic forces on fatigue life of marine risers, Journal of Sound and Vibration 329 (1) (2010) 43–55.

[17] M. Thorsen, S. Sævik, C. Larsen, Time domain simulation of vortex-induced vibrations in stationary and oscillating flows, Journal of Fluids and Structures 61 (2016) 1–19.

[18] M. Thorsen, S. Sævik, C. Larsen, Non-linear time domain analysis of cross-flow vortex-induced vibrations, Marine Structures 51 (2017) 134–151.

[19] J. Ulveseter, M. J. Thorsen, S. Sævik, C. M. Larsen, Time domain simulation of riser VIV in current and irregular waves, Marine Structures 60 (2018) 241–260.

[20] M. Thorsen, S. Sævik, C. Larsen, A simplified method for time domain simulation of cross-flow vortex-induced vibrations, Journal of Fluids and Structures 49 (2014) 135–148.

[21] M. J. Thorsen, S. Sævik, C. M. Larsen, Fatigue damage from time domain simulation of combined in-line and cross-flow vortex-induced vibrations, Marine Structures 41 (2015) 200–222.

[22] J. Ulveseter, S. Sævik, C. Larsen, Time domain model for calculation of pure in-line vortex-induced vibrations, Journal of Fluids and Structures 68 (2017) 158–173.

[23] H. Braaten, H. Lie, NDP Riser High Mode VIV Tests Main Report, Tech. Rep., Norwegian Marine Technology Research Institute, 2005.

[24] G. Baarholm, C. Larsen, H. Lie, On fatigue damage accumulation from in-line and cross-flow vortex-induced vibrations on risers, Journal of Fluids and Structures 22 (1) (2006) 109–127.

[25] T. L. Resvanis, J. Vandiver, Response variability in flexible cylinder VIV model test data, in: Proceedings of the ASME 2017 36th International Conference on Ocean, Offshore and Arctic Engineering, 2017.

[26] P. A. Brodtkorb, P. Johannesson, G. Lindgren, I. Rychlik, J. Ryden, E. Sjo, WAFO - A Matlab Toolbox for Analysis of Random Waves and Loads, in: International Offshore and Polar Engineering Conference, 2000.

[27] DNV GL, Recommeded Practice DNVGL-RP-0005:2014-06 RPC203: Fatigue design of offshore steel structures, Tech. Rep., 2014.

[28] P. K. Soni, Hydrodynamic Coefficients for Vortex-Induced Vibrations of Flexible Beams, Ph.D. thesis, University of Science and Technology, 2008.

[29] E. Huse, Ormen Lange 3D Model Tests Main Report, Tech. Rep., Norwegian Marine Technology Research Institute, 2001.

[30] B. M. Sumer, J. Fredsoe, Hydrodynamics Around Cylindrical Structures, Revised Edition, World Scientific Publishing Co. Pte. Ltd., 2006.

[31] S. B. Swithenbank, J. K. Vandiver, C. M. Larsen, H. Lie, Reynolds Number Dependence of Flexible Cylinder VIV Response Data, in: Proceedings of the ASME 27th International Conference on Offshore Mechanics and Arctic Engineering, 2008.